Composites Part B 266 (2023) 111038

Contents lists available at ScienceDirect

Composites Part B

journal homepage: www.elsevier.com/locate/composites

# Synchrotron micro-CT in kink-band formation of UD-CFRP laminates with microdefects

Jiraphant Srisuriyachot [a], Jean Bénézech [a], Guillaume Couégnat [b], Sophie A.M. McNair [a], Thomas Maierhofer [a], Richard Butler [a], Alexander J.G. Lunt [a,*]

[a] Centre for Integrated Materials, Processes & Structures (IMPS), Department of Mechanical Engineering, University of Bath, Bath, BA2 7AY, United Kingdom
[b] Laboratoire des Composites Thermostructuraux, UMR5801 CNRS/Univ. Bordeaux/Safran/CEA, 3 allée de la Boétie, 33600 Pessac, France

ARTICLE INFO

Dataset link: https://doi.org/10.15125/BATH-01313

*Keywords:*
A. Carbon fibre
B. Defects
C. Micro-mechanics
D. Non-destructive testing
Kink-band formation

ABSTRACT

This paper presents the first synchrotron micro-Computed Tomography (micro-CT) study on in-situ pure compressive kink-band failure in Uni-Directional Carbon Fibre-Reinforced Polymer composites (UD-CFRPs) with a notch. The study compares the failure behaviour of baseline samples under standard conditions with defect-rich samples containing micro-defects such as voids and fibre misalignment. Quantitative image-based analysis using the structure tensor technique and Digital Volume Correlation (DVC) reveals changes in fibre orientation and localised strain, respectively, at each increment load. A large 400 μm kink-band inclined at 30° with a half-cosine wave fibre orientation is observed in the baseline samples, while the defect-rich samples form narrower conjugate kink bands (ranging from 77 μm 25 μm) inclined at 45°. Development of kink-band formations/failure of both samples is discussed and compared with literature, providing key implications for the design and safe use of this type of composite layup.

## 1. Introduction

Carbon fibre-reinforced polymer (CFRP) composites are increasingly used in high-performance applications due to their exceptional combination of high stiffness and low density. For example, CFRP components have demonstrated significant performance improvements and are helping to reduce fuel consumption / $CO_2$ emissions in many sectors in pursuit of Net Zero emissions [1]. Despite these benefits, many composite parts are currently over-engineered due to poor failure load predictions which are driven by incomplete understanding of their complex damage mechanisms.

One such failure mechanism is kink-band formation, which is the primary compressive failure mode of Unidirectional (UD)-CFRP components. UD-CFRPs are predominantly used in systems with a preferred load orientation. Previous studies have suggested that this failure mode may be driven by fibre misalignment/waviness during layup or the shear yield strength of the matrix [2]. When the material is compressed, it locally deforms within a band which can be described in terms of a kink-band inclination angle ($\beta$) with respect to the transverse load direction, a band width ($\omega$) and fibre rotated angle ($\alpha$) relative to the global longitudinal direction. The formation and evolution of a kink-band can be split into three phases: (i.) initiation, in which a few fibres begin to kink within a band; (ii.) propagation, in which the band grows transversely and increases its width along the inclination angle $\beta$, and (iii.) broadening — in which the band grows axially, increasing its width along the fibre rotated angle $\alpha$.

The presence of microdefects is known to generate distinct kink-band failure modes [3]. One defect which is known to increase the severity of fibre kinking is voiding. These microdefects arise from incomplete consolidation during the curing process and can lead to a significant reduction in mechanical performance [4]. This is important as an average void content of 3% to 5% of matrix volume can be found in prepreg material which can lead to a compressive strength reduction of up to 40% [5]. Elastic modulus also shows a significant dependence on the void content, with a reduction of up to 12% [6]. Previous studies have assumed that the weakest point of a CFRPs under compression is where load-bearing layers contain the void with the longest unsupported neighbouring fibre [7]. This is believed to lead to stress concentration and fibre misalignment which are both known to promote kinking [8]. There is, however, very little experimental evidence of how CFRPs fails via kink-band formation. Therefore, the principal goal of this study is to characterise the formation of this band via in-situ high resolution analysis of representative CFRPs containing intentionally induced microdefects and compare that response to that observed under standard conditions.

*Abbreviations:* DVC, Digital Volume Correlation; FE, Finite Element

* Corresponding author.
*E-mail addresses:* js2580@bath.ac.uk (J. Srisuriyachot), ajgl20@bath.ac.uk (A.J.G. Lunt).

https://doi.org/10.1016/j.compositesb.2023.111038
Received 6 June 2023; Received in revised form 25 September 2023; Accepted 5 October 2023
Available online 10 October 2023

The aim of this work is to address this challenge by investigating the development of fibre kinking and the impact of microdefects on this phenomenon during in-situ compression of notched samples via Synchrotron X-ray Computed tomography (CT). This builds on the pioneering work of Wang et al. and other authors [9–14] who have studied alternative, un-notched geometries using Synchrotron CT. Additionally, this study will be the first to assess the local 3D strain in the microstructure using Digital Volume Correlation (DVC). This has been achieved by performing high resolution X-ray micro-CT of CFRP such that the fibres can be used as a tracking pattern. Particular focus has been placed on the different deformation response of the differing CRFP samples examined in this study.

## 2. Background

### 2.1. Experimental

Conventionally, kink-band formation can be generated by uni-axial compression. However, the unstable and rapid nature of this failure mode make the comprehension of the damage scenario/chronology challenging. Different sample geometries have been proposed in the literature in attempt to promote a stable fibre kinking failure mode such as a cylindrical rod specimen [9], a composite ring [15] and a rectangular sample with a notch [16,17]. However, a sudden and unstable fibre kinking failure were still observed in these experiments. In order to overcome this, and produce stable kink-band formation in a UD laminate, Volger and Kyriakides [17] applied combined compression and shear loading via a custom bi-axial testing device. This approach was extended by Pimenta et al. [18] who proposed a similar method to provoke stable kinking without the use of a custom device, but instead by the sample's geometry. In this arrangement, in-plane shear stress is generated in a notched sample by introducing a small fibre offset angle (from $\varphi = 0°$ to 4°) to the direction of compression, as shown in Fig. 1 . This approach was found to be particularly powerful in monitoring kink-band formation, although large amounts of misalignment were found to induce fibre splitting instead of kink-band formation [19]. This geometry effectively subdues the unstable failure and will therefore be used to incrementally study the formation of this response in the subsequent analysis.

The advancement of X-ray and detector technology has led to the routine use of micro-CT for the non-destructive reconstruction of the three-dimensional (3D) micro-structures of materials. However, micro-CT characterisation of CFRP remains challenging due to low phase contrast between fibre and epoxy matrix, which arises from the similarities in density and attenuation coefficients in the two phases [20]. Preliminary characterisation of the kink-band samples revealed that lab-based CT does not have sufficient phase contrast or spatial resolution to precisely identify individual fibres in a sample of representative size. However, synchrotron micro-CT of these samples offers significant potential to improve current understanding of kink-band formation. The associated phase-contrast analysis allows the interaction between voids, fibres and the matrix materials to be recorded, and the short exposure times mean that incremental time-resolved loading can be performed.

A powerful example of this approach was pioneered by Wang et al. who performed four-point testing of CFRP samples using Synchrotron micro-CT [9,10,13]. In this study, the evolution of fibre kinking was captured by micro-CT during in-situ loading. Although this method was able to resolve the internal structure, and provide unique insights into the formation of kink-bands in a qualitative manner, the four-point test geometry is challenging to scan with micro-CT, as during rotation the largest dimension of the sample is aligned with the incoming beam. This induces significant changes in the X-ray path length and attenuation, which influences the quality of the reconstruction and means that quantitative interpretation of the results via methods such as DVC are challenging.

In order to overcome this limitation and gain improved insights into the development of fibre kinking, a different geometry based on the work of Pimenta et al. [18,19] has instead been used in this study to capture CT images during in-situ loading. Importantly, the symmetry of the sample allows higher resolution, phase-contrast enhanced imaging to be performed during stable fibre kinking to be formed. Accordingly the high resolution, and high-contrast 3D reconstructions can be post-processed via image processing analysis such as Digital Volume Correlation (DVC) to study the internal behaviour of the parts and strain field development, as outlined below.

### 2.2. Digital volume correlation

DVC is a powerful analysis method to quantify the internal displacement field from high-resolution reconstructed micro-CT images, and thereby determine the strain induced between load increments. In this study the open-source DVC package kintsugi[1] was used. This DVC implementation is based on a global approach [21] in which the entire Volume-of-Interest (VOI) is considered and a shared set of parameters is used for displacement interpolation via a finite element (FE) mesh [22]. This ensures continuity in the resulting displacement field and overcomes the challenges associated with the use of multiple local VOIs, which can be difficult to reliably integrate into a final result when using a local approach [23,24]. Accordingly, despite sometimes being more processor intensive, the accuracy of the global DVC approach is typically much higher than a local equivalent [25–27].

In addition to local strain analysis, DVC can be used to characterise damage events such as cracks and fibre–matrix debonding which induce displacement field discontinuities in the deformed image that can be identified through the study of local residuals [28]. The use of a FE mesh also facilitates the comparison of the DVC results with FE simulations, which opens the way for the DVC to be used for validation or identification purposes [28–31].

## 3. Methodology

### 3.1. Sample preparation

All tests were conducted on 22 ply Hexcel UD AS4/8852 prepreg laminates with a stacking sequence of $[0_2/90/0_8]_s$. One batch of samples was made using the manufacturer's recommended autoclave curing cycle (at 180 °C and 7 bar for 2 h), and a second batch was made at a lower pressure (~ 2 bar) to deliberately induce defects, such as voids and fibre misalignment, in the sample. This approach has previously been successfully used by Hapke et al. [8,32] to study void induced strength changes in a UD CFRP laminate. Samples were sectioned into ~ 3 mm strips from a cured laminate plate of 15 mm × 3 mm × 4.4 mm.

The nature of low pressure consolidation of the laminate means that the generation of voids is random (not uniformly distributed across the laminate). However in order to study the impact of this phenomenon on the generation of kink-bands, precise determination of these features was required before the samples were machined in order to ensure the features were located in the region of interest. Therefore, lab-based CT was performed on the plates, which had sufficient contrast to identify the locations of the voids. These locations were subsequently used to choose where to cut samples to place the voids within FOV. Prior to the synchrotron experiment a second CT scan was performed on the sectioned samples to confirm that the voids were located within the VOI.

As outlined above, the focus of this study is on the influence of voiding in kink-band formation in UD composites. However, in order to reliably produce representative UD, it was necessary to add 90° plies on either surface to mitigate thermal warping during the consolidation

[1] https://gitlab.com/gcouegnat/kintsugi

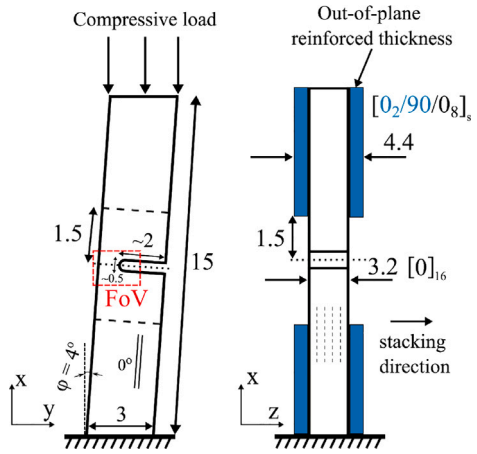


**Fig. 1.** Off-axis compression test (mm). The global out-of-plane reinforcements are shown in blue and the FOV is highlighted in red. (For interpretation of the references to colour in this figure legend, the reader is referred to the web version of this article.)

process. Once these samples had been manufactured, it was therefore necessary to remove these outer plies in order to leave a purely UD region for characterisation. Therefore, the central 3 mm × 3 mm of each laminate were subsequently machined on either surface to remove ~ 3 plies and leave a thickness of ~ 3.2 mm as shown in Fig. 1. It should be noted that this kink-band geometry was pioneered by Pimenta et al. [18] and is designed for the assessment of structures with a cross sectional ratio approximately equal to 1. The kink-band behaviour of this geometry differs to that of large aspect ratio, plate type structures in which the kink-band response is typically dominated by out-of-plane buckling [33]. As outlined above, the geometry used in this study preferentially induces in-plane buckling which has the added practical benefit of ensuring the VOI remains within the limited field of view offered by high resolution synchrotron CT. This is critical in ensuring that the deformation of the sample can be reliably captured, as required by the DVC characterisation performed.

In order to minimise the impact of this machining process on the kink-band response of the samples, the lab-based CT used to identify the voids within the samples was also used to assess the machining process. It was found that the tolerances of this process were within a few 10's of microns of each other and that in general a good quality machined surface had been achieved. The outliers of these samples were tested to determine the likely impact of machining on the kink-band response, and it was found that the surface roughness and amount of material removed had no perceivable impact on the failure load or mode. The samples used for the synchrotron study were then carefully selected to be those that were most precisely machined in order to minimise the influence of sample preparation on the results. It should be noted that sample preparation at the microscale is challenging and therefore minor differences are to be expected. However, despite this, it is noted that the chosen samples showed consistent and comparable effects, suggesting that these variations did not substantially impact the results obtained.

A length of 15 mm was selected as the nominal sample length, taking into account the need to avoid both Euler buckling and edge effects, as well as to ensure sufficient gauge area. In order to further isolate the location of the buckling response within the micro-CT VOI, a diamond wire saw with a ~ 0.5 mm diameter wire was used to cut a ~ 2 mm deep notch transverse to the fibre direction. Careful selection of this cutting depth was required to guarantee failure occurs gradually and within the loadcell capacity. Therefore preliminary FE simulations and testing were used to optimise this length.

As outlined above, fibre kinking is an unstable failure mode which can be controlled and gradually developed by offsetting the fibre direction with respect to the compressive load [18]. Recommendations for $\varphi$ are between 1° to 5°. In this case, $\varphi = 4°$ offset was selected based on the FE simulation which had the broadest non-linearity before failure. This offset angle was controlled by attaching EL2 epoxy/AT30 hardener resin blocks at the ends of the sample and polishing the sample ends at the designed angle using a specially produced in-house rig. This approach also ensured the boundaries were reliably clamped to avoid point loads and brooming at the ends [34].

### 3.2. Experimental setup

Micro-CT image acquisition was performed at the I13-2 beamline at Diamond Light Source. A pink beam of peak energy 19 keV was obtained through a series of Pyrolytic graphite filters and an aluminium filter, and the beam was collimated to 10 mm × 10 mm using beam-defining slits. The PCO.edge high speed 5.5 X-ray camera was used to capture radiographs at each load increment at a resolution of 2560 × 2560 px. Micro-CT data was collected via a flyscan over 180° at an increment of 0.01° (18,000 projections) with an exposure time of 50 ms. A ×2 objective lens was selected in addition to the detectors ×2 predefined magnification (×4 total magnification), resulting in a FOV of 4.2 mm × 3.5 mm with an effective pixel size of ~ 1.625 μm. This pixel size is sufficient to distinguish individual fibres with $\phi_f = \sim 7$ μm in diameter. To enhance the phase contrast between the fibres and matrix, an in-line phase propagation study was employed by collecting micro-CT data sets at a range of sample to detector distances [35]. The reconstructions were then analysed to determine an optimised sample-to-detector distance of 580 mm. A schematic representation of the synchrotron experiment is shown in Fig. 2.

A Deben CT5000 5kN load cell, co-axially fixed onto a tomography tower, was used to perform in-situ compressive testing of baseline and defect-rich samples. The tower was composed of an Aerotech goniometer, along with multiple Huber and Newport motors, to facilitate sample rotation and the translation required for synchrotron micro-CT at the location of interest. A compressive load was applied at a rate of 0.1 mm/min along the primary fibre axis of the sample. Micro-CT data were collected at each increment load while the motors held stationary, and the increment was reduced close to the expected failure loads for all samples until they failed. This ensured that the initiation of failure and subsequent failure (e.g. fibre kinking, matrix shear and fibre fracture) were captured during the experiment. The samples were held using steel grips that were able to load the sample via the resin blocks on either end. Estimates of the expected failure load were obtained by loading 10 nominally identical samples of each type before the start of the synchrotron experiment. These results were used to determine the load increments applied to the sample during the micro-CT study.

### 3.3. Image processing

#### 3.3.1. Image reconstruction

The parallel-beam tomography data collected at the synchrotron was reconstructed via a back projection algorithm implemented within Savu [37], which included dark- and flat-field correction. Ring artefact correction was performed to minimise artefacts in the micro-CT scans. The centre of rotation (COR) of the image was determined manually from an iterative process by processing a single slice in which the COR was iteratively shifted by 0.5 px. This allowed a visual determination of optimal COR, which overcomes some of the limitations of the automated process.

#### 3.3.2. Fibre orientation determination

Structure-tensor analysis was implemented on the micro-CT datasets collected at different load increments in order to estimate the fibre's orientation distributions and changes. The structure tensor can be defined as a product of $\nabla f \otimes \nabla f$ at each voxel, where $\nabla f$ is the image gradient computed from an optimal kernel for the fibres [26,38,39]. In order to determine the first order estimate of this structure tensor,

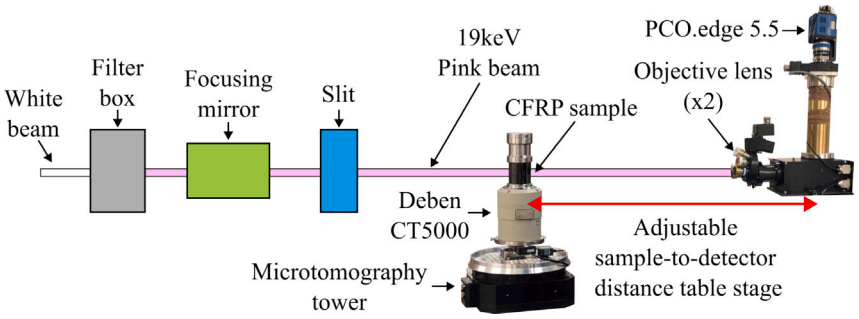


**Fig. 2.** Schematic setup of micro-CT at beamline I13-2 [36].

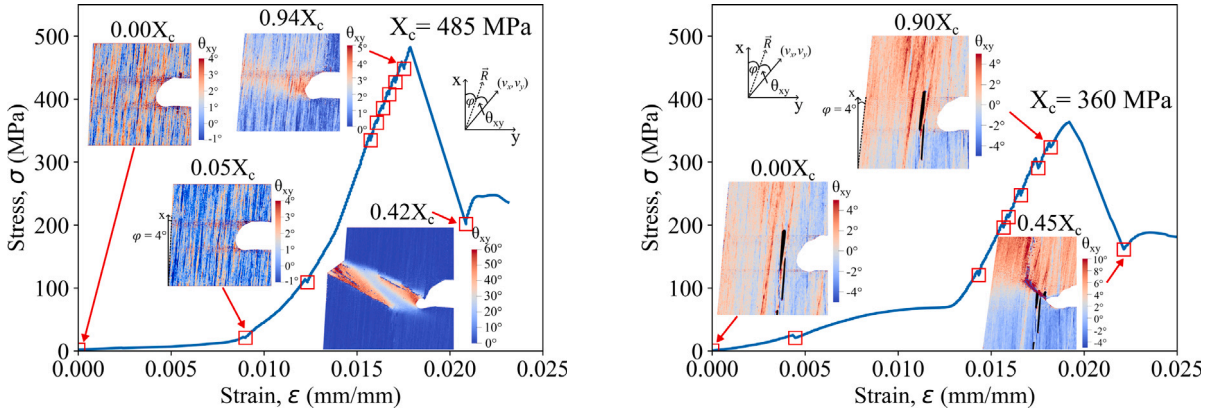


(a) Stress-strain plot: baseline sample #1

(b) Stress-strain plot: defect-rich sample #1

**Fig. 3.** Stress–strain plots of (a) baseline sample #1 and (b) defect-rich sample #1 along with its evolution of fibre orientation at initial loading, before and after failure. Incremental loading was performed to facilitate collect of micro-CT at the locations shown in red squares.

neighbouring voxels are convoluted with a Gaussian kernel to reduce noise and other artefacts which can significantly impact the estimates obtained. Optimisation of the kernel size was incrementally performed on the data set, in order to determine a value that effectively suppressed noise whilst not over smoothing the underlying data. From this analysis the optimal window size was determined to be 9 × 9 × 9 voxels. For a given voxel, the local orientation of the fibre corresponds to the eigenvector of the convoluted structure tensor with the smallest eigenvalue represented as a unit vector, $\vec{v} = (v_x, v_y, v_z)$. In other words, the direction of the smallest change in image gradient.

Two primary orientations were defined relative to the sample's coordinate system: the in-plane (xy) direction, perpendicular to the laminate stacking, and the out-of-plane (xz) direction, parallel to the stacking, as illustrated in Fig. 1. The fibre deflection angles, $\theta_{xy}$ and $\theta_{xz}$, were computed in terms of a relative angle between the fibre orientation vector $\vec{v}$ and the predefined fibre orientation used during manufacture, $\hat{R}$. As outlined above, the angular offset of $\hat{R}$ relative to the global coordinate system is $\varphi = 4°$ and $\psi = 0°$ for the xy and xz planes, respectively as shown in Appendix. The evolutions of fibre orientation at different loading stages of the baseline and defect-rich sample are shown in Fig. 3. A beam hardening artefact was induced in the micro-CT images by the notch, which led to increase noise at the crack tip, however the length scale of this phenomenon was found to be a few pixels and therefore had a minor influence on the reconstruction. Note: Stress, $\sigma$, is determined via $\sigma = \frac{P}{A_r}$, where $P$ is applied load and $A_r$ is the reduced cross-sectional area estimated from micro-CT image at the unloaded state. $X_c$ is maximum compressive stress achieved.

### 3.3.3. Void segmentation

The voids in the defect-rich sample were segmented via the imageJ [40] Plugin, MorphoLibJ [41]. This is a powerful and well-established approach for void identification [42,43] however, pre-processing is required to use this approach. In particular, a Gaussian filter was required to prevent misidentifying of fibres as a void, along with adjustment of the brightness range bounds. This allowed identification of the precise location, size and shape of each of the voids, and to compute the void volume fraction in the images. To determine the positions of the voids in 3D space, segmentation analysis was performed on the micro-CT images collected prior to loading and overlaid with fibre misalignment angles as shown in Fig. 4(a) and Fig. 4(b), respectively.

### 3.3.4. Digital volume correlation

The strain results were analysed to gain insights into the development of the kink-band prior to failure. Given that the combination of in-plane shear ($\epsilon_{xy}$) and compressive strain ($\epsilon_{xx}$) is expected to cause the fibre kink, these strains were selectively analysed and presented for both sample types. To perform the analysis, the DVC package kintsugi[1] was used to implement a global approach, which is summarised in Fig. 5. The unloaded micro-CT reconstructions of both samples were used as reference images, in which the grey-scale value at each voxel was denoted as $f(\mathbf{x})$. In order to reduce processing time and focus on the region of interest, a cuboidal VOI was cropped from this reconstruction. The subsequent deformed micro-CT reconstructions of the samples were denoted as $g(\mathbf{x})$, and the same regions of interest were obtained via cropping.

The dimensions of the VOI cuboids were defined to be 1300 × 1800 × 1200 voxels (2.0 × 2.7 × 1.8 $mm^3$) and 1000 × 2150 × 1200 voxels (1.5 × 3.2 × 1.8 $mm^3$) for the baseline and defect-rich samples, respectively. To facilitate the convergence of the DVC algorithm, a rough estimate of the displacement field was obtained from the load cell's motor travel distance. This estimate was further improved by computing a rigid body registration using a phase correlation approach in the Fourier space [44,45]. The FE meshes of the VOI are obtained thanks to an image-based Delaunay refinement algorithm available in CGAL [46]. A binary mask of the VOI is obtained by thresholding

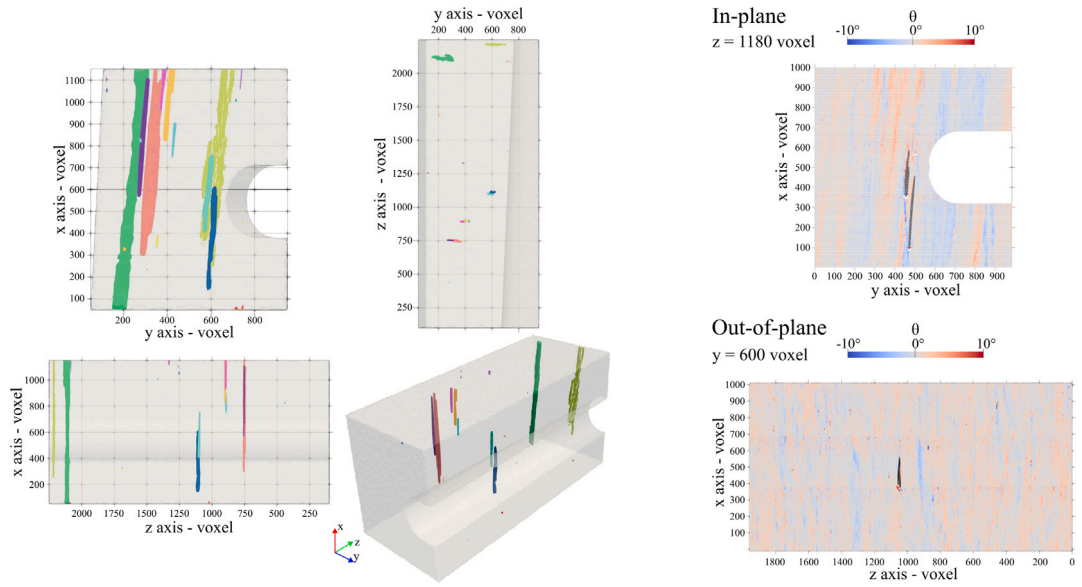


(a) Void Segmentation (b) Fibre misalignment

**Fig. 4.** (a) Positions and shapes of voids in the defect-rich sample #1. The total void volume fraction was estimated to be 0.2% from micro-CT image within the VOI. Individual voids were colour-coded to indicate disconnectedness from neighbouring voids. (b) Illustration of a cross-sectional slice showing fibre misalignment due to presence of voids: in-plane direction, xy, and out-of-plane direction, xz.

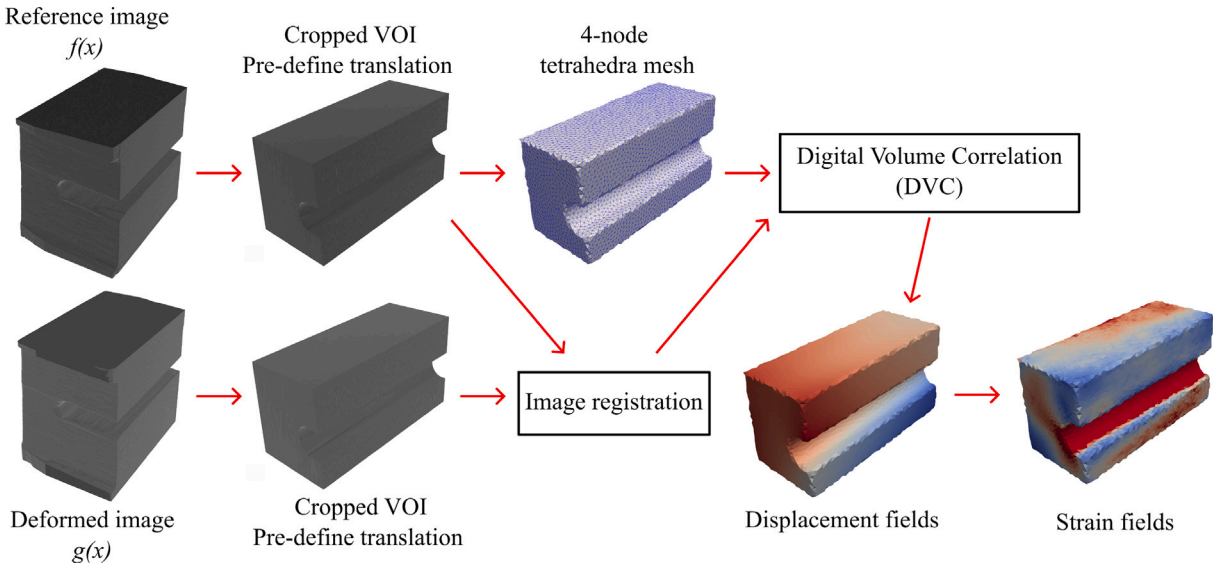


**Fig. 5.** Overview of global DVC approach.

the micro-CT in the reference state and excluding the notch region. A further 50 px (~ 80 μm) were removed from the edges of the VOI to accommodate the anticipated displacement of the specimen. This binary representation was subsequently converted to a 3D unstructured tetrahedral mesh using CGAL. The selection of mesh size, $l_{mesh}$, is also crucial as large elements will be less subjected to noises because of large number of voxels involved in each element, but it is unable to capture complex displacement fields. On the other hands, a small $l_{mesh}$ will be flexible enough to follow large displacement gradients, but it will be more subjected to the noises. The $l_{mesh}$ is recommended to be at least 3 to 5 times larger than the $l_c$ to have enough texture within each element allowing the DVC to converge. As a result, the smallest $l_{mesh}$ used in this study is 32 px.

After the rigid body motion has been corrected, the DVC algorithm computes the displacements at each vertex of the tetrahedral mesh. One of the most challenging aspects of DVC analysis is to deal with the ill-posedness/conditioned nature of image correlation. In the present study, a "mechanical" regularisation approach [47] was used to help with the convergence of the Newton–Raphson iteration process and to ensure smoothness of the solution. The weight of the regularisation is introduced through the choice of a so-called regularisation length $l_{reg}$. As a rule of thumb, $l_{reg}$, should be at least twice the $l_{mesh}$ [47] and much larger than the correlation length of the image, $l_c$, to achieve a reliable solution. In this study, the $l_c$ or texture pattern for DVC analysis is the random distribution of individual fibre diameter $\phi_f = 7$ μm, determined to be ~ 5 px. Thus, the sensitivity will be studied by adjusting $l_{mesh}$ and $l_{reg}$ in the following. Fig. 6 illustrates the sensitivity analysis of both sample types with different $l_{mesh}$ and $l_{reg}$ values, namely as (a) localised, (b) intermediate and (c) global deformation. It should be noted that the smoothness of the strain field increases with higher $l_{reg}$, as well as decreasing the image noises dependency to the computed result.

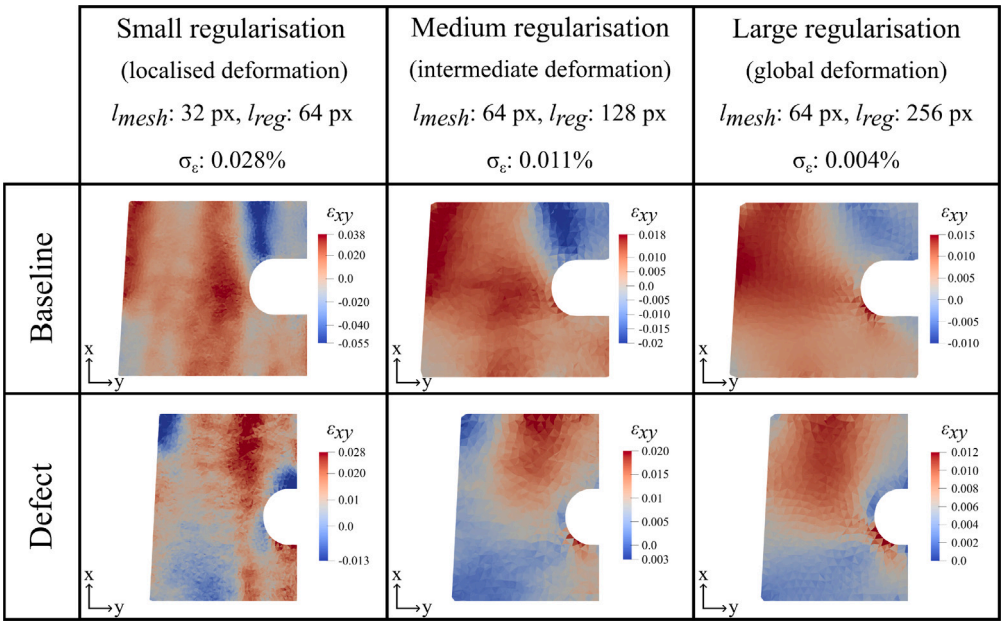


**Fig. 6.** Illustration of shear strain, $\epsilon_{xy}$ sensitivity and measured strain uncertainty, $\sigma_\epsilon$, obtained from DVC analysis of the baseline and defect-rich sample. The continuity of the $\epsilon_{xy}$ increases while $\sigma_\epsilon$ decreases from left to right as the regularisation value, $l_{reg}$, is increased. The $l_{reg}$ of 64 px, 128 px and 256 px were defined as small, medium and large regularisation to capture localised, intermediate and global deformation of the materials.

It is important to note that as well as changing the length scales over which the DVC is sensitive, changing the values of $l_{mesh}$ and $l_{reg}$ influences the uncertainty of the results. The degree of measured strain uncertainty, $\sigma_\epsilon$, was determined to be 0.028%, 0.011% and 0.004% for the localised, intermediate and global deformations respectively. These levels are well within the uncertainty expected of this type of analysis [21]. Accordingly, it is clear that the localised analysis, $l_{reg}$ of 64 px, is suitable for examining small scale effects, at the cost of having low confidence in bulk behaviour. In contrast, there is more confidence in the global response at a $l_{reg}$ of 256 px but this is unable to detect localised effects. However, these displacement fields are still essential to determine the overall kinking response and input boundary conditions for FE simulations [48].

Careful interpretation of the DVC can, in some cases, be used to determine an incremental estimate of the bulk strain of the sample and correct for factors such as compliance of a load rig. The key requirement for this type of correction is the analysis of a VOI that is representative of the sample as a whole. In the case of this study, preference was given to maximising the resolution of the CT to ensure that reliable tracking of the fibres was possible and explore the localised effects induced by kinking. Given that the number of pixels on a given detector is limited, this naturally leads to a smaller VOI which was highly localised to the notch. This in turn meant that the strain estimates from the VOI were found to be representative of the global response for the first few loading states. After this point, the impact of the notch and formation of the kink-band dominated the strain measure and therefore this approach could not be used to reliably correct for load cell compliance. Accordingly, a decision was made to present strain values obtained from the load cell, with the caveat that this is likely to be influenced by compliance as shown in Fig. 3(a) and Fig. 3(b).

## 4. Results and discussion

A different failure mechanism was observed between the baseline and defect-rich samples. The main coincident damage features in both sample types were characterised in Fig. 7 and are summarised in Table 1. It should be noted that no voids were detected inside the baseline samples at the resolution achieved in this study.

**Table 1**
Kink-band parameters measured from the baseline and defect-rich samples; * was measured between the upper and lower kink-edges, and † was measured between adjacent kink-edges (as shown in Fig. 7).

| Parameters | Baseline | Defect-rich |
|---|---|---|
| Band angle ($\beta$) - ° | 30 | 45 |
| Band width ($w$) - μm | 400*/55† | 77 to 25 |
| Fibre rotation ($\alpha$) - ° | 25–60 | 85 |

### 4.1. Baseline sample

Prior to the loading of the baseline sample, the fibres were found to have a minor misorientation with respect to the direction of the prescribed $\varphi$ angle, as shown in Fig. 3(a). This is due to the positional settling of the sample and the compliance of the loadcell. After the load is applied and this compliance is accounted for, the fibres began to align with the $\varphi$ at a load $0.05X_c$ and elastic deformation is observed. This linear relationship is observed up to a point where a small region of material behind the notch begins to deform inelastically (at a load of between 0.3 - $0.4X_c$). As outlined by Moran et al. [16] this is likely associated with local fibres bending towards the notch (positive angle) which leads to a significant increase of shear strain within the band. The matrix becomes stiffer which locks the fibres in place and determines the band angle $\beta$. This concentrated localised shear strain is clearly indicated by the DVC analysis and is the first experimental evidence to support this formation route. These deflected fibres lead to fibre instability and provoke the early stages of kink band formation. This early inelastic deformation was referred to as "incipient kinking" by Moran et al. [16]. Following continued loading, fibre rotation continues up to ~ +5° at a load of $0.94X_c$. This lays the foundations for the subsequent failure and means that band broadening becomes the easiest deformation mode to accommodate the overall end-shortening of the sample. The bent fibres at the kink-edge spread outward into the unkinked area which remains soft in shear, resulting in near instantaneous propagation into the kink-band. Unfortunately, the rapid nature of this failure mode means that micro-CT could not be collected between $0.94X_c$ and $X_c$. However, the scans prior to this point reveal progressive fibre reorientation towards a kink-band which validates the mechanism of formation proposed by Moran et al..

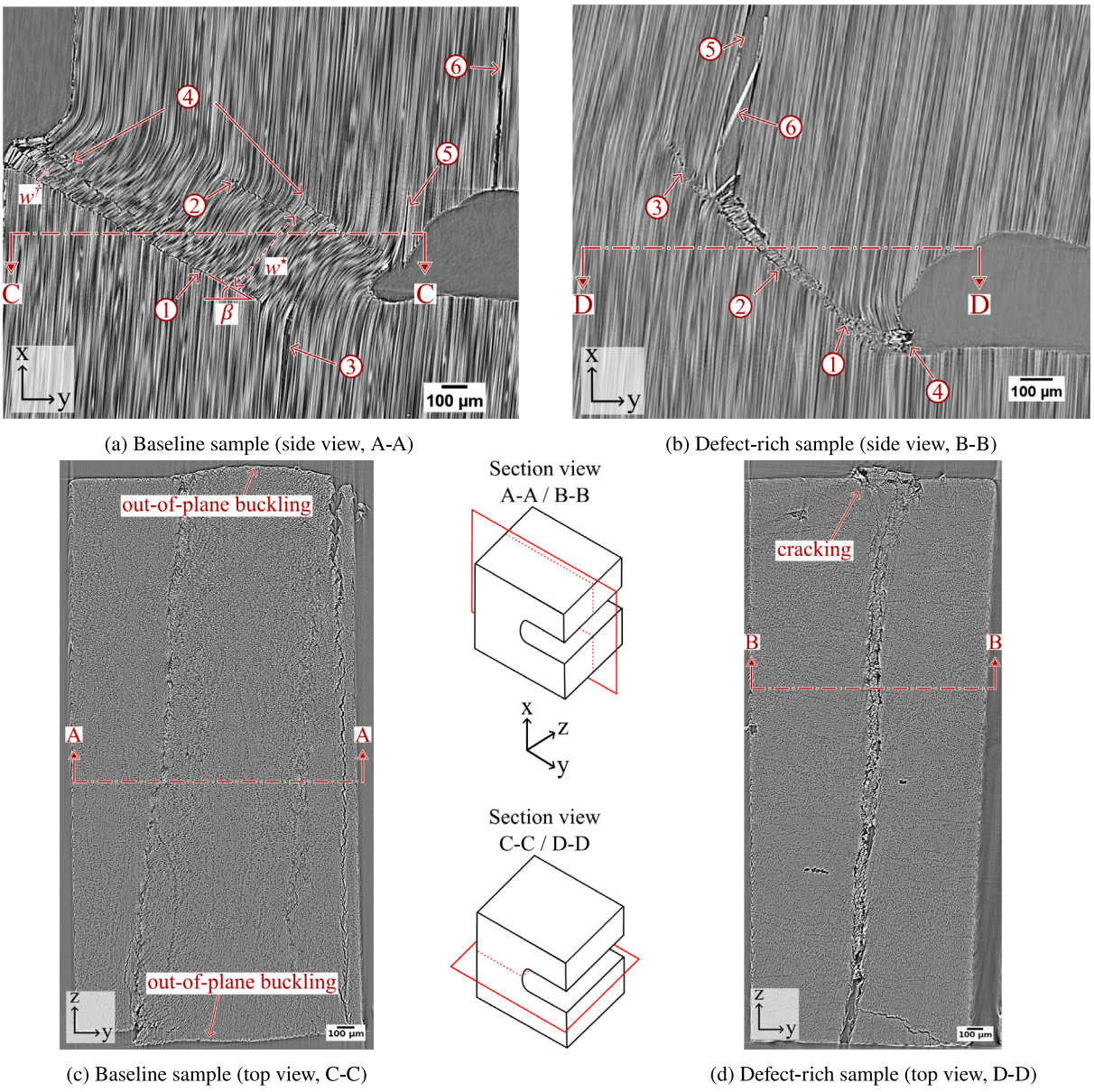


**Fig. 7.** Example of micro-CT slices showing kink-bands after failure in the two samples. (a) Section view A-A of baseline sample shows the following features ① - ②: lower/upper boundary of kink-band ③: Long fibre–matrix debonding, ④: multiple kink-bands ⑤: fibre splitting due to notch sensitivity ⑥: Pre-existing damage. (b) Section view B-B of defect-rich sample: ① - ②: convergence kink-bands, ③: micro kink-band ④: crushed wedge-shaped kink-band, ⑤: matrix cracking and/or fibre–matrix debonding, ⑥: fibre bridging. (c) Section view C–C of the baseline sample with fibre buckling out-of-plane visible on free surfaces. (d) Section view D-D of the defect-rich sample with matrix cracking and a reduced amount of out-of-plane fibre buckling on free surfaces.

After failure, fibres inside the large kink-band bent uniformly up to ~ +60° and formed a half cosine-wave, while fibres outside the band remained straight along the original 4° angle at the fracture plane. The unbroken fibre was deflected up to ~ +25°. As depicted in Fig. 7(a), a macro kink-band with a uniform width of ($w \sim 400\,\mu m$) propagates across the width of the sample at an average angle of $\beta \sim 30°$. The band width after failure was found to be larger than that previously observed in compression tests, however it is within the range observed in kink-band shear studies (up to ~ 2030 μm with a bi-axial device) [17,19]. This suggests that the application of shearing increases the band width and confirms the conclusions of Pimenta et al. [19]. It should be noted that the width of this kink-band was measured following strain localisation and the load maximum.

It should be noted that quantification of the magnitude of these analytical forces remains challenging, and therefore the precise relationship between shear force and band width remains unclear. The primary reason for this is that analytical methods are unable to reliably capture the relaxation induced by the incipient damage prior to failure, which reduces the magnitude of the shear force prior to kink band formation by an amount that, as of yet, has not been determined. One route to quantify this effect is the use of DVC guided FEA of the sample, however this analysis requires an assessment of the entire structure. As outlined above the focus of this study was enhancing understanding of the microstructure of kink-band formation so we prioritised resolution over the size of the field of view. Accordingly quantifying the global shear strain and impact of this on the band formation was not possible due to the localised effects within the region captured. Despite this, a subsequent study in which the external shear force magnitude is recorded and the entire sample is tracked using enhanced contrast DVC is planned, which would be able to quantify the relationship between shear force and kink-band in an effective manner.

Partial fibre fracture (label ①) formed at the lower edge of the kink-band and propagated across the sample. Fibres bending without

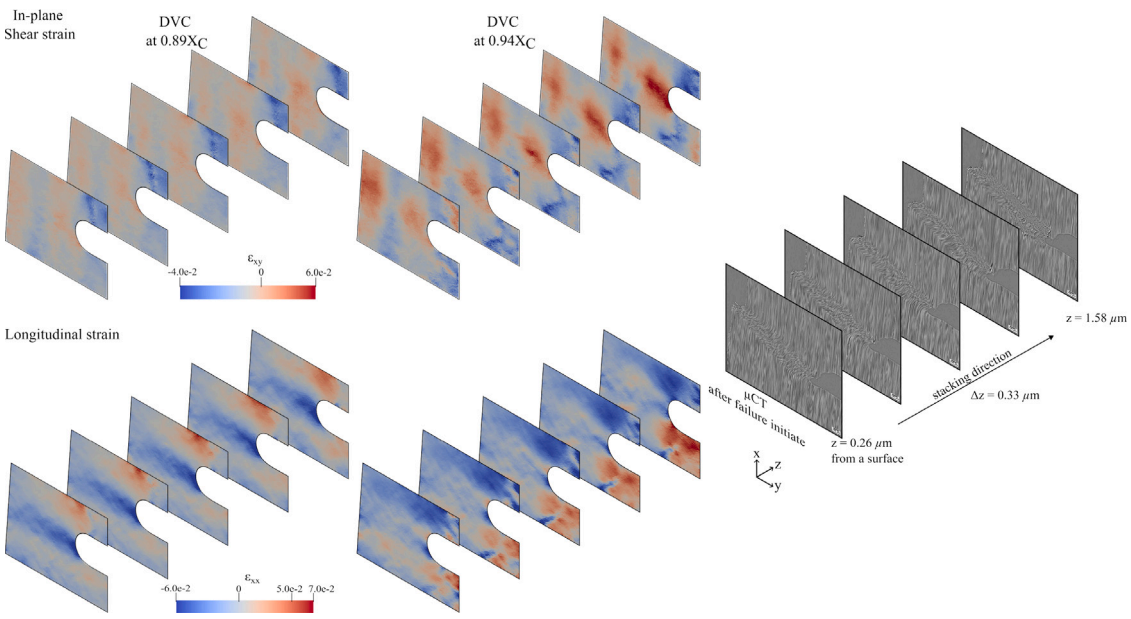


**Fig. 8.** Comparison between the localised DVC strain mapping in the initial half thickness at the final two increments, $0.89X_c$ and $0.94X_c$ and micro-CT after failure in the baseline sample. Please see the loading plot in Fig. 3(a) for reference.

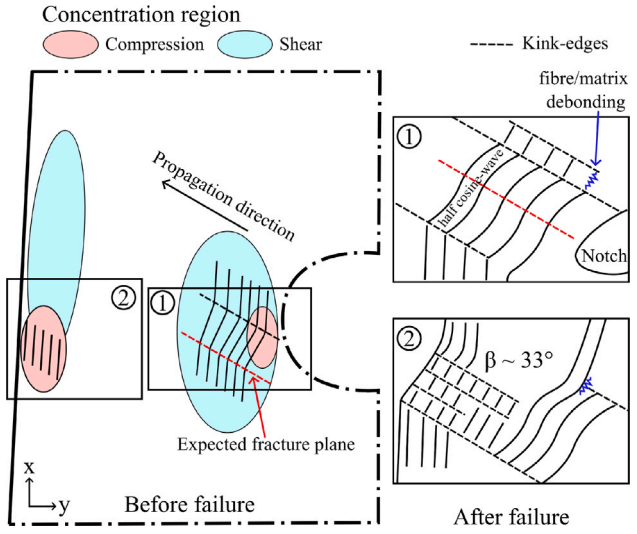


**Fig. 9.** Schematic diagrams of local strain concentrations and transition of kink-band development before and after failure in baseline sample. Note that the compression and shear concentration are approximately from Fig. 8.

failure was observed on the upper kink-edge on the surfaces along with numerous incidences of fibre–matrix debonding (label ②). However, micro-CT revealed that this partial fibre fracture only occurred in the sub-surface regions. At the tips of the fractures, fibre–matrix debonding was observed, creating a potential area for the fibre to bend or rotate, leading to the formation of a kink-band. A long region of fibre–matrix debonding (label ③) located below the notch was also observed. Close examination of the micro-CT reconstructions at unloaded state shows a small step in the sample surface opposite to the notch which could have acted as a secondary notch in the sample. Multiple small kink-bands (label ④) were observed in this region with partial fibre fractures propagated across the sample. Unlike the above macro kink-bands, these kink-bands widths $w$ were determined to be ~ 55 μm.

Label ⑤ shows imperfections around the vicinity of the notch that resulted in fibre splitting during loading which is related to the notch sensitivity observed in UD composites. Pre-delamination was found to already exist from the cutting the notch, as shown by label⑥. Out-of-plane fibre buckling was also observed at edges of the sample on the top cross-sectional slice of the micro-CT, as shown in Fig. 7(c). The average maximum out-of-plane deformation was determined to be ~ 60 μm accounting to be 1.7% of the sample thickness. However, the geometrical constraints present within the centre of the sample, prevented this effect from occurring in this region.

A non-uniform distribution of in-plane strain can be observed behind the notch in the baseline sample. This corresponds to a stress concentration which varies in the through-thickness direction, such that one side of the sample is strained more than the other, as shown by the DVC results in Fig. 8. This could also be correlated with the out-of-plane deformation which can be observed in Fig. 7(c). It is important to note that the magnitude of this response is substantially smaller than that which would be expected during out-of-plane buckling and is a localised deformation response which has previously been observed in the literature [49]. As outlined above, sample preparation led to minor changes in the geometry of the sample and therefore small variations in strains are expected. However, a noticeable compressive local extreme of strain is also observed above the notch. This is related to a existing pre-crack that opens continuously during the loading, but does not interfere with the kink band formation.

Although DVC analysis was performed at each load increment, the inhomogeneous strain distribution was not observed until 300 N had been applied (corresponding to 100 MPa in Fig. 3(a)). This indicates that below this force, the compliance of the rig dominates strain accommodation. A focal point of strain concentration was detected behind the notch that propagated within the sample during the application of load. It should be noted that the DVC prior to failure was sufficient to predict the inclination angle of the kink $\beta$, based on prior models, and throughout this process the compressive strain intensified and remained confined to the area around the notch. The combination of maximum shear strains and fibre deflection ahead of the notch pre-defined the upper surface of the kink. Compressive strain concentrations were also observed on the opposite side of the sample to the notch, at which the lower edge of the kink band was generated.

A combined schematic view of the localised strain mapping and fibre deflection results for the baseline sample is shown in Fig. 9. At the point where the fibres bend the most, highly compressive strain is induced on one side of the individual fibres [50], in addition to the

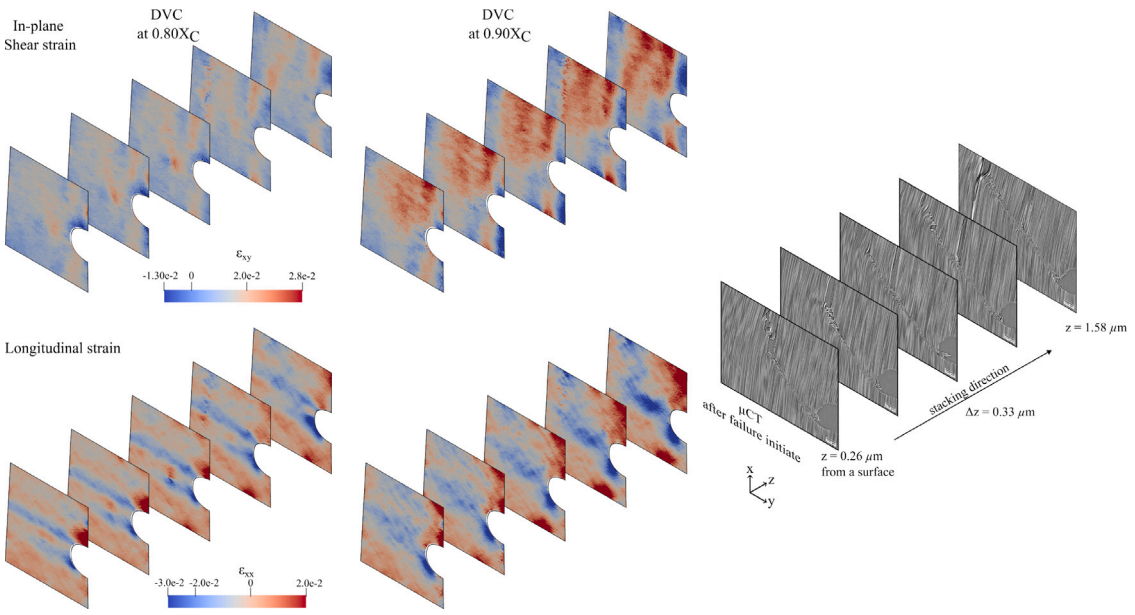


**Fig. 10.** Comparison between the localised DVC strain mapping in the initial half thickness at the final two increments, $0.80X_c$ and $0.90X_c$ and micro-CT after failure in the baseline sample. Please see the loading plot in Fig. 3(b) for reference.

existing axial compressive strain [51,52]. These results in fibre fracture which propagated along the kink-edge. Fibre–matrix debonding is also observed above the fracture, allowing the fibres to bend even further, generating another kink-edge. The position of the lower kink-edge could be considered as independent from the upper-kink edge as both originate from locations of strain concentration prior to failure; ① one at the notch and ② one at the free edge in Fig. 9. This fracture on the lower kink-edge disturbs the fibre orientation on the upper kink-edge and results in a large half cosine-wave which has not been observed elsewhere. Once the fibres are relieved from this strain concentration, they remained locked in position, meaning that the fracture plane would not occur at the position expected prior to failure as shown in Fig. 9 ①. Therefore, the resulting shape of the kink-band suggests that the lower kink-edge likely initiated prior to the upper kink-edge.

It is interesting to note that multiple kink-bands were also observed on the surface of a kink-band sample by [53] using SEM. This suggests that fibre fracture and the formation of a small wedge leads to two zones of tensile and compressive stress on the fibre surface and that fibre bending failure originated from instability. The broadening multiple kink-bands, shown in Fig. 9 ②, have also been previously reported to be necessary to accommodate the time-dependent behaviour of the polymer matrix and are believed to be energetically more favourable in terms of generate new kink-bands in the soften regions of the sample, in preference to the existing band [8].

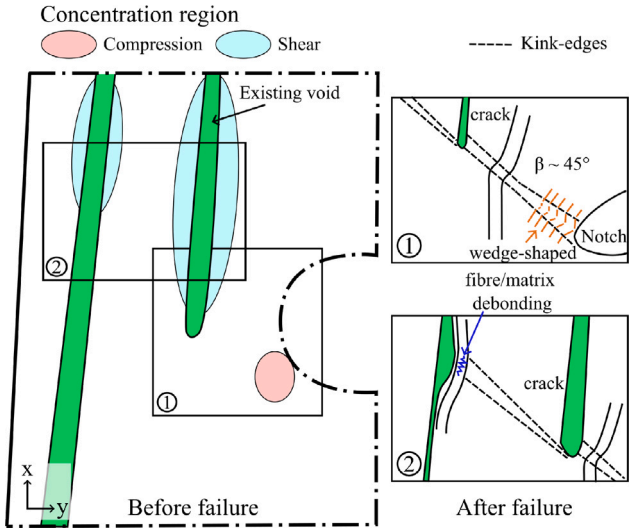


**Fig. 11.** Schematic diagrams of local strain concentrations and transition of kink-band development before and after failure in defect-rich sample in vicinity of notch. Note that the compression and shear concentration are approximately from Fig. 10.

### 4.2. Defect-rich sample

Fibre orientation and void segmentation analysis enable the quantitative assessment of microscale fibre misalignment due to the existing voids in the CFRP sample, see Fig. 3(b) and Fig. 4. This analysis reveals that micro-voids impose severe fibre misalignment, deviating fibres by up to ± 5° from $\varphi$ prior to the loading, $0.00X_c$. These fibres were deviated by voids kept their orientation tangent to the voids' end caps shape. This created a propagation of misalignment in the distant vicinity of the voids, resulting in global fibre misalignment in the defect-rich sample. Furthermore, these deviated fibres generated localised densely packed of fibres regions, which lead to stress heterogeneity. Through an examination of fibre misalignment density in in-plane (xy) and out-of-plane (xz), it was found that the misalignment distribution in the xy plane was likely to be greater than that in the xz plane. The voids were observed to have an oval shape, flattened in the lamina plane elongating in fibre direction. This suggested that voids are likely to grow transversely to the external pressure application during the consolidation and that the void arose from existing resin rich pockets in the laminate. The severity of the fibre misalignment increased at locations where multiple voids were present as shown in Fig. 4(b). The void volume fraction of the defect-rich sample was calculated from the micro-CT of the VOI and was determined to be ~ 0.2%. It is important to note that the resolution of the scan places a lower limit on the resolution of voids which can be detected at 625 nm, and therefore nanovoids may be present within the system which have not been included in this estimate. Comparisons between this measure and macroscale equivalents of void fraction are also challenging due to the substantially different size of the gauge volumes associated with these measures.

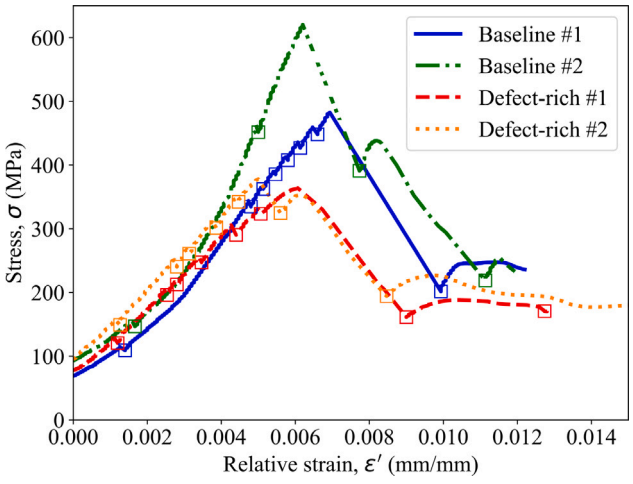


(a)

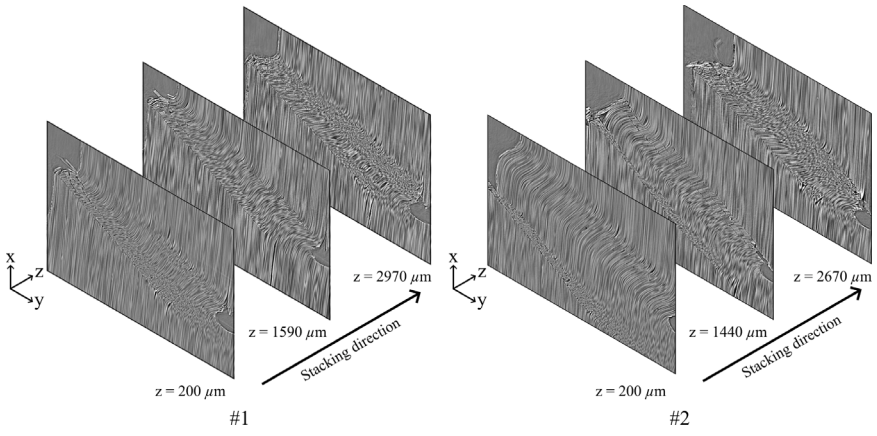


(b) Baseline samples micro-CTs

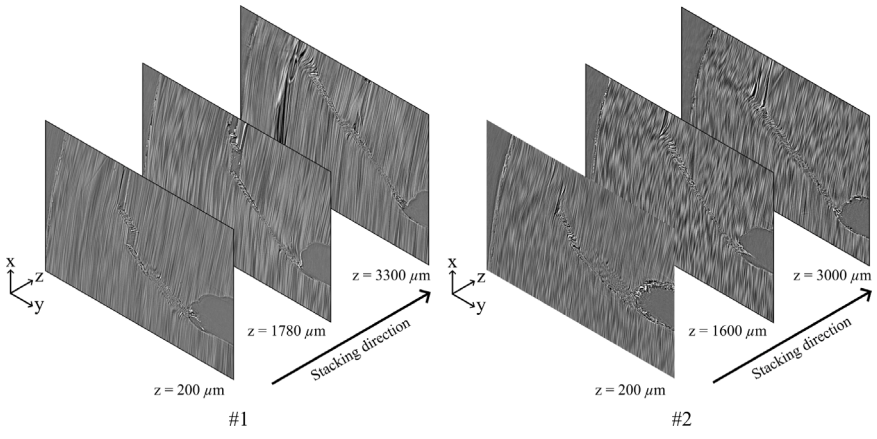


(c) Defect-rich samples micro-CTs

**Fig. 12.** Illustration of (a) stress-relative strain plot of two baseline and defect-rich samples repeated under in-situ loading; Incremental loading was performed at each of the locations of square boxes to facilitate micro-CT shown. (b) - (c) micro-CT images of kink-band formation of the repeated samples showing one ply below the surfaces and the mid-thickness of the sample.

As was observed in the baseline sample, Fig. 3(b) reveals that for the defect-rich sample, linear elastic deformation occurs after accommodation of the compliance load (at approximately $0.2X_c$). In contrast to the baseline sample the first non-linearity is observed close to the failure point at approximately $0.80X_c$. At this point, the DVC reveals the generation of two distinct fibre deflection regions above and below the notch, rather than behind the notch (as in the baseline sample). The rotation and localised strain at these locations increase in magnitude up to a load of $0.90X_c$. Upon reaching the critical failure load $X_c$ these two regions of localised strain connect via a kink-band. The severity of the fibre deflection after failure was found to be as high as $\sim 10°$ in the upper region, whereas below the notch deflections were observed up to $\sim -4°$. This contradicts the kinking kinematic assumptions of Budiansky and Fleck (1993) [54], which assume no fibre rotation

outside the band. However, the relationship between the inclination angle ($\beta$) and the fibre rotated angle ($\alpha$) follows the usual pattern, such that $\alpha = 2\beta$ [16,55]. It is important to note that in this experiment, the upper region of the sample experiences significant deformation and rotation prior to crack appearance and therefore the assumption on which this analytical model was developed are no longer relevant. In contrast, this assumption remains valid for a baseline sample in which no deformation or rotation was observed in either end of the sample.

The micro-CT image of the defect-rich sample is shown in Fig. 7(b). Within this image labels ① - ② indicate fully defined kink-edges which converged $w$ from 77 μm to 25 μm with $\beta \sim 45°$. This convergent band width has been also described in terms of a pair of conjugate kink-bands with inclined fracture planes form in opposite directions [13,56]. These broken fibres were observed to be 0° to 35° out-of-plane, depending on the localised area. A small and narrow kink-band was identified behind the fibre–matrix debonding which inclined in the same angle as the previous dominant band, see label ③. This kink-band also propagated to another existing void/crack in other section view #1 in Fig. 7(b). Wedge-shaped kink-bands were observed at the notch tip where the fibres were buckled and crushed as shown in label ④. In addition to kink-bands, matrix cracking and/or fibre–matrix debonding (label ⑤) along with fibre bridging within the crack (label ⑥) were also observed. This crack propagated across the sample thickness and is likely to have originated from the existing void near the surface, as shown in Fig. 7(d).

Due to the sudden failure of the materials, it remains challenging to determine precisely the initial mode of failure using solely the micro-CT image observation. For instance, one cannot conclude whether failure originates from fibre kinking or matrix cracking and/or fibre–matrix debonding. In order to establish more confidence in the likely failure sequence, DVC analysis was subsequently conducted on the data set to observe the strain evolution prior to failure.

In contrast to the baseline sample, Fig. 10 indicates that shear strain was concentrated above the notch of the defect-rich sample at a location where matrix cracking and fibre–matrix debonding occurred. Further strain concentrations were observed around the longest unsupported region, which was above the locations of voids. In comparison, the magnitude of strain concentration behind the notch was found to be much less significant than that compared to the baseline sample. This DVC result suggests that the origin of failure in the defect-rich sample was matrix cracking and fibre–matrix debonding. Following this initial failure, a reduction in cross sectional area led to a increased concentration of stress. The resulting bending triggered kink-band formation at a stress/strain magnitude smaller than the baseline sample with 26% material strength reduction based on sample #1 for both types.

Following the first initiation failure (matrix cracking), it is believed that kink-band formation was induced by the deflection of the fibres from the tip of the splitting area to the traction free space where the laminate was still intact and acting as a stress concentration point. This led to a loss of fibre stability and induced a transverse tensile strain in the matrix leading to fibre–matrix debonding. Eventually the bending angle reached a threshold value which caused the fibre to break [7,57] as shown in Fig. 11 ②. Deformation of a single fibre with and without a laterally supported region, due to the existing voids or matrix cracking. The narrower kink-band in this sample occurs at an angle of 45° suggesting that the fibres close to the voids were compressed and bent along a shear crack (shear-dominant) as previously observed by [50,58]. However, these voids and associated longitudinal splitting are also believed to stop the growth of the fibre micro-buckling by absorbing energy and delaying failure [13]. For example, Hapke et al. [8] found that the presence of a void arrested kink-band propagation by bringing the inner surfaces of the void into contact. However, confirmation of this behaviour remains challenging as it depends on the precise size/position of the void and localised stress.

### 4.3. Repeatability of compressive testing

During the synchrotron experiment two baseline and two defect-rich samples were studied. As outlined above during the initial stages of loading a degree of compliance was observed as the samples 'settled in'. The displacement associated with this differed between samples, however the magnitude at which sample loading was initiated and a distinct change of gradient was observed was consistent at approximately 100 N for all samples. Accordingly, in order to facilitate more effective comparison between the samples a relative strain ($\epsilon'$) was determined by setting the displacement to zero at 100 N. The stress-relative strain plots are shown in Fig. 12(a). the point at which the samples began to bear the load, with respect to sample nominal length for an ease of comparison between samples. In all samples, the unstable failure mechanisms were not fully suppressed, as demonstrated by the sudden load drops. These plots show a minor decrease in stress (10–30 MPa) when the sample was held stationary for the collection of the micro-CT data. This effect was particularly prevalent at larger loads and was likely to be evidence of geometric softening of the material due to the viscoelastic response of the matrix [8].

Due to the time limitations associated with the synchrotron experiment, the repeat baseline and defect-rich samples could not be scanned at as many load increments as the initial iterations. This difference in the number and therefore total duration of the holding period led to increased geometric softening of these samples due to the viscoelastic nature of CFRPs, as has previously been observed in the literature [8]. This resulted in some discrepancy in the apparent stiffness of the two baseline samples. However, the same macro kink-bands with a half-cosine wave can still be observed (Fig. 12(b)). For the defect-rich sample, the stress–strain plot (Fig. 12(a)) and micro-CT images (Fig. 12(c)) showed stronger similarities, due to the lower loads and reduced relaxation induced. Once again, for these samples nominally identical results were observed in terms of the failure mechanisms, albeit with minor variations due to void size / location and boundary conditions.

## 5. Conclusion

The internal deformation and damage mechanisms associated with UD-CFRP kink-band formation under in-situ pure compression were successfully recorded and analysed in 3D to reveal the internal local strain development for the first time. Both standard (baseline) and non-standard curing pressures (defect-rich) were studied to ascertain the effect of micro-defects, such as voids and fibre misalignment, on this compressive failure responses. It has been shown that the in-situ micro-CT is able to overcome the limitations associated with surface observation and post-mortem analysis of this failure mode, which have been found to be unrepresentative of the bulk material. Detailed damage characteristics and a failure sequence have been determined and corroborated via previous observations in the literature. For example the quantitative image-based DVC performed was able to identify the development of kink-band formation through-thickness in the CFRP. Based on this, it can be concluded that the formation of kink bands in CFRPs can happen in two distinct scenarios, case 1 is prevalent in a defect-free system and case 2 occurs when voids and fibre misalignment are present within the gauge volume

Case 1: the application of compressive and shear loads cause the fibres to bend towards the notch and generate significant shear strain. This results in an increase in shear stiffening resistance in the matrix, caused fibre lock-up and thereby established the band inclination angle. The bent fibres then propagated into the neighbouring unkinked region, ultimately leading to fibre fracture when the maximum bending stress was achieved. This approach serves as the first experimental validation of Moran's kinematic theory [16] in terms of strain analysis, and the fibre rotations required to form a kink band. Fibre–matrix debonding was also observed at the fibre fracture plane, creating a potential area

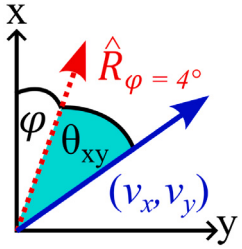


(a) In-plane orientation

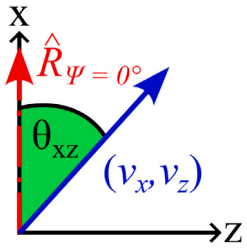


(b) Out-of-plane orientation

**Fig. A.1.** Definition of (a) in-plane, $\theta_{xy}$, and (b) out-of-plane, $\theta_{xz}$, fibre deflections in a two dimensional Cartesian coordinate system. A unit vector, $\hat{R}$, represents a prescribe angle in each orientation while $\varphi = 4°$ in the xy-plane and $\psi = 0°$ in the xz-plane. The $\theta_{xy}$ and $\theta_{xz}$ are determined as the difference between the prescribed angles ($\varphi$ or $\psi$) and the fibre orientation vector, $\vec{v} = (v_x, v_y, v_z)$, from the structure tensor analysis.

for the fibre to bend or rotate, leading to the formation of a kink-band. A uniform through-thickness kink-band (roughly ~ 400 μm band width inclined at 30°) were determined in this sample. It appears that the fibre orientation formed a half-cosine wave within the band which suggested two independent fibre kinking area and fracture planes that occurred after fibre lock-up during shear stiffening.

Case 2: microdefects can have a substantial impact on the global response of the sample. In this study, the defect-rich sample largely deformed and induced matrix cracking as an initiation failure at the existing void near surface, and propagated across the sample thickness before leading to the early kink-band formation. Fibres lost lateral support due to the preformed crack or existing voids leading to severe fibre instabilities, in addition to the fibre misalignment (up to ± 5°) due to voids. This in turn leads to the formation of kink bands at substantially lower stresses with 26% material strength reduction under 0.2% void volume faction of the sample. Conjugate kink-bands were formed with a band width ranging from ~ 77 μm to 25 μm and inclined at 45°. A wedge-shaped kink-bands was also observed at the notch tip. The sequential kink initiation location could not be determined as it could initiate at several different locations such as a void, matrix cracking and notch which then converged rapidly upon failure.

Accordingly, these two scenarios resulted in distinct failure mechanisms in the two sample types in this study. The results of this study therefore provide key insights into understanding the kink-band formation in CFRPs with and without microdefects. This is crucial in developing more accurate kink damage criteria and facilitating more accurate modelling in the future. Further, the application of this methodology to samples of this type provide a powerful new methodology to facilitate future study in this area. Ultimately, both outcomes will lead to the powerful new insights and capabilities required to more reliably predict CFRP performance and thereby reduce over engineering of this widely used material class.

## CRediT authorship contribution statement

**Jiraphant Srisuriyachot:** Conceptualisation, Data analysis, Investigation, Methodology, Sample preparation, Writing – original draft. **Jean Bénézech:** Conceptualisation, Data analysis, Supervision, Writing – review & editing. **Guillaume Couégnat:** Data analysis, Software, Supervision. **Sophie A.M. McNair:** Investigation. **Thomas Maierhofer:** Investigation. **Richard Butler:** Conceptualisation, Supervision, Writing – review & editing. **Alexander J.G. Lunt:** Conceptualisation, Supervision, Methodology, Writing – original draft, Writing – review & editing.

## Declaration of competing interest

The authors declare that they have no known competing financial interests or personal relationships that could have appeared to influence the work reported in this paper.

## Data availability

Datasets related to this article can be found at https://doi.org/10.15125/BATH-01313, hosted at Bath: University of Bath Research Data Archive [59].

## Acknowledgements

This work was supported by the UKRI - Engineering and Physical Sciences Research Council, United Kingdom, Grant 'Certification for Design - Reshaping the Testing Pyramid' EP/S017038/1. Jiraphant Srisuriyachot is funded by GKN Aerospace, United Kingdom. The Diamond Light Source is acknowledged for providing the beamtime on I13-2 beamline under the experiment number MG28362-2.

## Appendix. Fibre orientation definition

Fig. A.1(a) illustrates the definition of fibre deflection in the in-plane, $\theta_{xy}$, and Fig. A.1(b) out-of-plane, $\theta_{xz}$, directions. Unit vectors denoted as $\hat{R}$ refer to the predefined fibre orientations during manufacture. This is associated with an offset of $\varphi = 4°$ in the xy-plane in accordance with the offset loading geometry and $\psi = 0°$ in the xz-plane. For each fibre the offsets $\theta_{xy}$ and $\theta_{xz}$ were determined by the mismatch between the prescribed angles ($\varphi$ or $\psi$) and the fibre orientation vector, $\vec{v} = (v_x, v_y, v_z)$, which was obtained from the structure tensor analysis in each direction.

## References

[1] Department for Energy Security and Net Zero and Department for Business, Energy & Industrial Strategy. Net zero strategy: Build back greener. 2023, Available at: https://www.gov.uk/government/publications/net-zero-strategy.
[2] Argon A. Fracture of composites. In: Treatise of materials science and technology. vol. 1, New York: Academic Press; 1972, p. 79–114.
[3] Hahn HT, Williams JG. Compression failure mechanisms in unidirectional composites. ASTM International WestConshohocken, PA; 1986, http://dx.doi.org/10.1520/STP35345S.
[4] Liu L, Zhang B-M, Wang D-F, Wu Z-J. Effects of cure cycles on void content and mechanical properties of composite laminates. Compos Struct 2006;73(3):303–9. http://dx.doi.org/10.1016/j.compstruct.2005.02.001.
[5] Foye R. Compression strength of unidirectional composites. In: 3rd and 4th aerospace sciences meeting. 1966, p. 143.
[6] Schultheisz CR, Waas AM. Compressive failure of composites, part I: Testing and micromechanical theories. Prog Aerosp Sci 1996;32(1):1–42. http://dx.doi.org/10.1016/0376-0421(94)00002-3.
[7] Liebig WV, Viets C, Schulte K, Fiedler B. Influence of voids on the compressive failure behaviour of fibre-reinforced composites. Compos Sci Technol 2015;117:225–33. http://dx.doi.org/10.1016/j.compscitech.2015.06.020.
[8] Hapke J, Gehrig F, Huber N, Schulte K, Lilleodden E. Compressive failure of UD-CFRP containing void defects: In situ SEM microanalysis. Compos Sci Technol 2011;71(9):1242–9. http://dx.doi.org/10.1016/j.compscitech.2011.04.009.
[9] Wang Y, Soutis C, Withers P. Time-lapse X-ray microtomographic imaging of compressive failure in carbon fibre-epoxy composites. In: 20th International conference on composite materials, copenhagen, denmark. 2015.

[10] Wang Y. Damage mechanisms associated with kink-band formation in unidirectional fibre composites [Ph.D. thesis], The University of Manchester; 2016, p. 208, URL https://www.proquest.com/dissertations-theses/damage-mechanisms-associated-with-kink-band/docview/2022994100/se-2.

[11] Masahito Ueda KM, Jeong T-K. In situ observation of kink-band formation in a unidirectional carbon fiber reinforced plastic by X-ray computed tomography imaging. Adv Compos Mater 2016;25(1):31–43. http://dx.doi.org/10.1080/09243046.2014.973173.

[12] Emerson MJ, Wang Y, Withers PJ, Conradsen K, Dahl AB, Dahl VA. Quantifying fibre reorientation during axial compression of a composite through time-lapse X-ray imaging and individual fibre tracking. Compos Sci Technol 2018;168:47–54. http://dx.doi.org/10.1016/j.compscitech.2018.08.028.

[13] Wang Y, Chai Y, Soutis C, Withers PJ. Evolution of kink bands in a notched unidirectional carbon fibre-epoxy composite under four-point bending. Compos Sci Technol 2019;172:143–52. http://dx.doi.org/10.1016/j.compscitech.2019.01.014.

[14] Takahashi T, Todoroki A, Kawamura C, Higuchi R, Sugiyama T, Miyanaga T, Hattori K, Ueda M, Yokozeki T, Honda M. Unidirectional CFRP kinking under uniaxial compression modeled using synchrotron radiation computed tomography imaging. Compos Struct 2022;289:115458. http://dx.doi.org/10.1016/j.compstruct.2022.115458.

[15] Kyriakides S, Arseculeratne R, Perry E, Liechti K. On the compressive failure of fiber reinforced composites. Int J Solids Struct 1995;32(6):689–738. http://dx.doi.org/10.1016/0020-7683(94)00157-R, Time Dependent Problems in Mechanics.

[16] Moran P, Liu X, Shih C. Kink band formation and band broadening in fiber composites under compressive loading. Acta Metall Mater 1995;43(8):2943–58. http://dx.doi.org/10.1016/0956-7151(95)00001-C.

[17] Vogler T, Kyriakides S. On the axial propagation of kink bands in fiber composites : Part i experiments. Int J Solids Struct 1999;36(4):557–74. http://dx.doi.org/10.1016/S0020-7683(98)00029-8.

[18] Pimenta S, Gutkin R, Pinho S, Robinson P. A micromechanical model for kink-band formation: Part I — Experimental study and numerical modelling. Compos Sci Technol 2009;69(7):948–55. http://dx.doi.org/10.1016/j.compscitech.2009.02.010.

[19] Pimenta S. Micromechanics of kink-band formation [Ph.D. thesis], 142, Faculty of Engineering, University of Porto & Imperial College London; 2008.

[20] Sencu R, Yang Z, Wang Y, Withers P, Rau C, Parson A, Soutis C. Generation of micro-scale finite element models from synchrotron X-ray CT images for multidirectional carbon fibre reinforced composites. Composites A 2016;91:85–95. http://dx.doi.org/10.1016/j.compositesa.2016.09.010.

[21] Buljac A, Jailin C, Mendoza A, Neggers J, Taillandier-Thomas T, Bouterf A, Smaniotto B, Hild F, Roux S. Digital volume correlation: review of progress and challenges. Exp Mech 2018;58(5):661–708. http://dx.doi.org/10.1007/s11340-018-0390-7.

[22] Roux S, Hild F, Viot P, Bernard D. Three-dimensional image correlation from X-ray computed tomography of solid foam. Composites A 2008;39(8):1253–65. http://dx.doi.org/10.1016/j.compositesa.2007.11.011, Full-field Measurements in Composites Testing and Analysis.

[23] Forsberg F, Sjödahl M, Mooser R, Hack E, Wyss P. Full three-dimensional strain measurements on wood exposed to three-point bending: analysis by use of digital volume correlation applied to synchrotron radiation micro-computed tomography image data. Strain 2010;46(1):47–60. http://dx.doi.org/10.1111/j.1475-1305.2009.00687.x.

[24] van Dijk NP, Wu D, Persson C, Isaksson P. A global digital volume correlation algorithm based on higher-order finite elements: Implementation and evaluation. Int J Solids Struct 2019;168:211–27. http://dx.doi.org/10.1016/j.ijsolstr.2019.03.024.

[25] Dall'Ara E, Barber D, Viceconti M. About the inevitable compromise between spatial resolution and accuracy of strain measurement for bone tissue: A 3D zero-strain study. J Biomech 2014;47(12):2956–63. http://dx.doi.org/10.1016/j.jbiomech.2014.07.019.

[26] Mazars V, Caty O, Couégnat G, Bouterf A, Roux S, Denneulin S, Pailhès J, Vignoles GL. Damage investigation and modeling of 3D woven ceramic matrix composites from X-ray tomography in-situ tensile tests. Acta Mater 2017;140:130–9. http://dx.doi.org/10.1016/j.actamat.2017.08.034.

[27] Mao L, Liu H, Lei Y, Wu J, Ju Y, Chiang F-P. Evaluation of global and local digital volume correlation for measuring 3D deformation in rocks. Rock Mech Rock Eng 2021;54(9):4949–64. http://dx.doi.org/10.1007/s00603-021-02517-9.

[28] Mazars V, Caty O, Couégnat G, Bouterf A, Roux S, Denneulin S, Pailhès J, Vignoles GL. Damage investigation and modeling of 3D woven ceramic matrix composites from X-ray tomography in-situ tensile tests. Acta Mater 2017;140:130–9. http://dx.doi.org/10.1016/j.actamat.2017.08.034.

[29] Besnard G, Hild F, Roux S. "Finite-element" displacement fields analysis from digital images: application to Portevin–Le Châtelier bands. Exp Mech 2006;46(6):789–803. http://dx.doi.org/10.1007/s11340-006-9824-8.

[30] Avril S, Bonnet M, Bretelle A-S, Grédiac M, Hild F, Ienny P, Latourte F, Lemosse D, Pagano S, Pagnacco E, et al. Overview of identification methods of mechanical parameters based on full-field measurements. Exp Mech 2008;48(4):381–402. http://dx.doi.org/10.1007/s11340-008-9148-y.

[31] Shakoor M, Buljac A, Neggers J, Hild F, Morgeneyer TF, Helfen L, Bernacki M, Bouchard P-O. On the choice of boundary conditions for micromechanical simulations based on 3D imaging. Int J Solids Struct 2017;112:83–96. http://dx.doi.org/10.1016/j.ijsolstr.2017.02.018.

[32] Olivier P, Cottu JP, Ferret B. Effects of cure cycle pressure and voids on some mechanical properties of carbon/epoxy laminates. Composites 1995;26:509–15. http://dx.doi.org/10.1016/0010-4361(95)96808-J.

[33] Wilhelmsson D, Mikkelsen L, Fæster S, Asp L. Influence of in-plane shear on kink-plane orientation in a unidirectional fibre composite. Composites A 2019;119:283–90. http://dx.doi.org/10.1016/j.compositesa.2019.01.018.

[34] Srisuriyachot J, McNair SA, Chen Y, Barthelay T, Gray R, Bénézech J, Dolbnya IP, Butler R, Lunt AJ. Carbon fibre lattice strain mapping via microfocus synchrotron X-ray diffraction of a reinforced composite. Carbon 2022;200:347–60. http://dx.doi.org/10.1016/j.carbon.2022.08.041.

[35] Mayo SC, Stevenson AW, Wilkins SW. In-line phase-contrast X-ray imaging and tomography for materials science. Materials 2012;5(5):937–65. http://dx.doi.org/10.3390/ma5050937.

[36] Rau C, Wagner UH, Vila-Comamala J, Bodey A, Parson A, García-Fernández M, De Fanis A, Pešić Z. Imaging in real and reciprocal space at the Diamond beamline I13. AIP Conf Proc 2016;1696(1). http://dx.doi.org/10.1063/1.4937541.

[37] Wadeson N, Basham M. Savu: A python-based, MPI framework for simultaneous processing of multiple, N-dimensional, large tomography datasets. 2016, http://dx.doi.org/10.48550/arXiv.1610.08015, arXiv preprint arXiv:1610.08015.

[38] Mulat C, Donias M, Baylou P, Vignoles G, Germain C. Optimal orientation estimators for detection of cylindrical objects. Signal Image Video Process 2008;2(1):51–8. http://dx.doi.org/10.1007/s11760-007-0035-2.

[39] Bénézech J, Couégnat G. Variational segmentation of textile composite preforms from X-ray computed tomography. Compos Struct 2019;230:111496. http://dx.doi.org/10.1016/j.compstruct.2019.111496.

[40] Schindelin J, Arganda-Carreras I, Frise E, Kaynig V, Longair M, Pietzsch T, Preibisch S, Rueden C, Saalfeld S, Schmid B, et al. Fiji: an open-source platform for biological-image analysis. Nature Methods 2012;9(7):676–82.

[41] Legland D, Arganda-Carreras I, Andrey P. MorphoLibJ: integrated library and plugins for mathematical morphology with ImageJ. Bioinformatics 2016;32(22):3532–4. http://dx.doi.org/10.1093/bioinformatics/btw413.

[42] Watanabe T, Takeichi Y, Niwa Y, Hojo M, Kimura M. Nanoscale in situ observations of crack initiation and propagation in carbon fiber/epoxy composites using synchrotron radiation X-ray computed tomography. Compos Sci Technol 2020;197:108244. http://dx.doi.org/10.1016/j.compscitech.2020.108244.

[43] Jung S, Sabharwal M, Jarauta A, Wei F, Gingras M, Gostick J, Secanell M. Estimation of relative transport properties in porous transport layers using pore-scale and pore-network simulations. J Electrochem Soc 2021;168(6):064501. http://dx.doi.org/10.1149/1945-7111/ac03f2.

[44] Barros F, Sousa PJ, Tavares PJ, Moreira PM. A DFT-based method for 3D digital image correlation. Procedia Struct Integr 2017;5:1260–6. http://dx.doi.org/10.1016/j.prostr.2017.07.100, 2nd International Conference on Structural Integrity, ICSI 2017, 4–7 September 2017, Funchal, Madeira, Portugal.

[45] Rao KR, Kim DN, Hwang JJ. Fast fourier transform: algorithms and applications. vol. 32, Springer; 2010, http://dx.doi.org/10.1007/978-1-4020-6629-0.

[46] Wadeson N, Basham M. Computational geometry algorithms library. URL https://www.cgal.org.

[47] Mendoza A, Neggers J, Hild F, Roux S. Complete mechanical regularization applied to digital image and volume correlation. Comput Methods Appl Mech Engrg 2019;355:27–43. http://dx.doi.org/10.1016/j.cma.2019.06.005.

[48] Buljac A, Shakoor M, Neggers J, Bernacki M, Bouchard P-O, Helfen L, Morgeneyer TF, Hild F. Numerical validation framework for micromechanical simulations based on synchrotron 3D imaging. Comput Mech 2017;59(3):419–41.

[49] Wind JL, Waas AM, Jensen HM. Initiation of failure at notches in unidirectional fiber composites. Compos Struct 2015;122:51–6. http://dx.doi.org/10.1016/j.compstruct.2014.11.043, URL https://www.sciencedirect.com/science/article/pii/S0263822314006126.

[50] Gutkin R, Pinho S, Robinson P, Curtis P. On the transition from shear-driven fibre compressive failure to fibre kinking in notched CFRP laminates under longitudinal compression. Compos Sci Technol 2010;70(8):1223–31. http://dx.doi.org/10.1016/j.compscitech.2010.03.010.

[51] Pinho S, Darvizeh R, Robinson P, Schuecker C, Camanho P. Material and structural response of polymer-matrix fibre-reinforced composites. J Compos Mater 2012;46(19–20):2313–41. http://dx.doi.org/10.1177/0021998312454478.

[52] Wang Y, Emerson MJ, Conradsen K, Dahl AB, Dahl VA, Maire E, Withers PJ. Evolution of fibre deflection leading to kink-band formation in unidirectional glass fibre/epoxy composite under axial compression. Compos Sci Technol 2021;213:108929. http://dx.doi.org/10.1016/j.compscitech.2021.108929.

[53] Wang Y, Burnett TL, Chai Y, Soutis C, Hogg PJ, Withers PJ. X-ray computed tomography study of kink bands in unidirectional composites. Compos Struct 2017;160:917–24. http://dx.doi.org/10.1016/j.compstruct.2016.10.124.

[54] Budiansky B, Fleck N. Compressive failure of fibre composites. J Mech Phys Solids 1993;41(1):183–211. http://dx.doi.org/10.1016/0022-5096(93)90068-Q.

[55] Chaplin CR. Compressive fracture in undirectional glass-reinforced plastics. J Mater Sci 1977;12(2):347–52. http://dx.doi.org/10.1016/0266-3538(92)90080-M.

[56] Liu G, Thouless M, Deshpande V, Fleck N. Collapse of a composite beam made from ultra high molecular-weight polyethylene fibres. J Mech Phys Solids 2014;63:320–35. http://dx.doi.org/10.1016/j.jmps.2013.08.021.

[57] Vogler T, Kyriakides S. Initiation and axial propagation of kink bands in fiber composites. Acta Mater 1997;45(6):2443–54. http://dx.doi.org/10.1016/S1359-6454(96)00350-3.

[58] Pinho S, Gutkin R, Pimenta S, De Carvalho N, Robinson P. On longitudinal compressive failure of carbon-fibre-reinforced polymer: from unidirectional to woven, and from virgin to recycled. Phil Trans R Soc A 2012;370(1965):1871–95.

[59] Srisuriyachot J, Bénézech J, McNair SA, Maierhofer T, Butler R, Lunt AJ. Dataset for Synchrotron micro-CT in kink-band formation of UD-CFRP laminates with microdefects, Bath: University of Bath Research Data Archive, Version 1; 2023. http://dx.doi.org/10.15125/BATH-01313.